PCCP

ROYAL SOCIETY OF CHEMISTRY

TUTORIAL REVIEW

View Article Online
View Journal | View Issue

Cite this: *Phys. Chem. Chem. Phys.*, 2023, **25**, 30099

Rashba effect: a chemical physicist's approach

Maciej J. Szary

Understanding the mechanisms underlying the emergence of giant spin splitting (GSS) is fundamental in the pursuit of more robust strategies for designing materials with desired spin splitting. This drive for material innovation continues to captivate a burgeoning community of early-career researchers with backgrounds in chemistry and material science. However, new to the field, they are often equipped only with the insight provided by the original Bychkov–Rashba model. Furthermore, daunted by the tight-binding perspective on the non-vanishing orbital angular momentum (OAM), they struggle to accurately account for the atomic spin–orbit interaction (SOI) in the formation of GSS. To address these challenges and equip young chemists with better-suited tools, this review aims to provide a more intuitive perspective on atomic interactions (orbital hybridization), structure symmetry, and atomic SOI in the formation of GSS. In pursuit of this goal, the review explores the Bychkov–Rashba model, its advantages, and limitations. Subsequently, it introduces the orbital framework, wherein GSS is modulated by atomic SOI and the interplay of OAM with the surface electrostatic field. Given the explicit dependence of both these factors on OAM, the review examines why OAM is typically quenched in crystal structures and how chemical bonds involving different orbital types can lead to its non-zero values in the presence of inversion symmetry breaking. Finally, with this chemistry-focused perspective, the review examines the rise of GSS in selected examples.

Received 1st September 2023,
Accepted 30th October 2023

DOI: 10.1039/d3cp04242a

rsc.li/pccp

1 Why do we care?

The field of electronics is currently confronted with a multitude of challenges that have necessitated the exploration of innovative solutions capable of overcoming the limitations posed by traditional silicon-based technologies.[1–4] One such promising solution is spintronics. It represents a paradigm shift from traditional electronics, as it hopes to harness not only the electronic charge but also its spin angular momentum (SAM or simply spin) as an additional degree of freedom.[5–8] This novel approach holds profound implications for data storage and processing efficiency, promising the development of significantly faster devices capable of operating under minimal power consumption, provided its full potential is harnessed. The pursuit of spintronics has led to substantial progress in both theoretical and experimental domains. However, several critical technological challenges still remain unresolved. These obstacles must be addressed to fully realize the transformative impact of spintronics on the future of electronics.

The successful integration of spintronics with current fabrication technology poses an ongoing challenge, necessitating the development of semiconductor-based devices capable of generating spin-polarized electrons at room temperature.[9,10] One promising approach to address this problem involves the utilization of spin-polarized electrical injection from ferromagnets.[11,12] However, the challenging obstacles of spin lifetime and electron diffusion length still need to be addressed for the practical adoption of this method. Alternatively, another avenue pursued for semiconductor devices is the implementation of spin filtering and the generation of spin-polarized currents based on the Rashba spin-splitting effect.[13,14] For a spintronic application of the Rashba effect, three requisites must be met:

(i) a large spin splitting of
(ii) a metallic surface band on
(iii) a semiconductor surface.

The importance of the first and second requisites lies in facilitating substantial spin transport, while the third requisite is necessary due to the potential interference of large bulk currents in metallic substrates, which could obscure surface spin signals.

The fulfillment of these requisites holds promise for the advancement of spintronics in semiconductor devices, generating significant interest in materials exhibiting giant spin splitting (GSS). However, while Rashba-like physics is currently thriving among condensed matter physicists,[15–19] who are extensively studying non-equilibrium mechanisms like spin-to-charge conversion and nonlinear transport effects, chemists and material scientists often encounter difficulties in predicting the

---

Institute of Physics, Poznan University of Technology, ul. Piotrowo 3, 61-138 Poznan, Poland. E-mail: maciej.szary@put.poznan.pl

effects of structural functionalization or when describing the mechanisms behind the induced spin splitting. This poses a pertinent challenge for the development of spintronics due to an ever-growing demand for a comprehensive understanding linking the chemical modification of surfaces with the underlying physics, evident from the continuously increasing number of studies focusing on material modification for GSS modulation.

As such, this tutorial review hopes to bridge the gap between the chemistry and physics of spin–orbit interaction (SOI) induced GSS, providing an essential introduction to this topic. By elucidating the role of atomic interactions in the emergence of spin splitting, it endeavors to equip researchers with the necessary tools to address problems related to material modification for spintronic applications. This chemical perspective should have particular appeal to early career researchers, as well as established scientists seeking new fields to explore. To the best of the author's knowledge, this is the first review serving such a purpose, as previous works have predominantly focused on current developments from a physicists perspective.[14,19–23] To further help readers, Table 1 presents a glossary of terms commonly encountered in studies on spin splitting. The first instance of each term used in the text is highlighted in bold for additional ease of reference.

2 Bychkov–Rashba picture

Considering the common challenges associated with interpreting and describing the mechanisms responsible for spin splitting in surface systems, it is prudent to begin the discussion by reviewing the original model proposed by Bychkov and Rashba,[24] commonly known as the Rashba, BR, or RB model. It has a prominent presence in condensed-matter physics and spintronics courses, serving for decades as the foundational framework for describing the spin splitting of surface bands. One of its notable advantages is its relative simplicity, requiring only a modest background in quantum and relativistic physics, while still successfully predicting aspects of the phenomenon such as spin-degeneracy lifting with a chiral spin structure.[13,25–28] As a result, it often becomes the primary tool for early-stage researchers or scientists transitioning into the field from material science and chemistry-focused backgrounds. However, it is important to acknowledge that this simplicity also gives rise to limitations, leading to difficulties in interpretation and potential confusion.

To gain insight into the microscopic origin of Rashba-type spin splitting within the RB model, let us consider a fictitious system in the form of an *ideal* two-dimensional electron gas (2DEG) confined to the (x, y) plane (see Fig. 1a). Since the 2DEG is free from any crystal potential or electron–electron interactions, its Hamiltonian ($\hat{H}_{\mathrm{2DEG}}$) consists solely of the kinetic energy operator ($\hat{T}$), which, in turn, involves the momentum operator ($\hat{\boldsymbol{p}}$) and the electron mass (m_{e}) as denoted by the formula

$$\hat{H}_{\mathrm{2DEG}} = \hat{T} = \frac{\hat{\boldsymbol{p}}^2}{2m_{\mathrm{e}}}. \tag{1}$$

In such a case, the electron energy in 2DEG (E_{2DEG}) exhibits a quadratic dispersion with respect to its momentum, and the wavevector $\boldsymbol{k}$ ($\boldsymbol{p} = \hbar\boldsymbol{k}$),

$$E_{\mathrm{2DEG}}(\boldsymbol{k}) = \frac{\boldsymbol{p}^2}{2m_{\mathrm{e}}} = \frac{\hbar^2\boldsymbol{k}^2}{2m_{\mathrm{e}}}. \tag{2}$$

As a result, the electronic bands of the 2DEG take on characteristic parabolic shapes (see Fig. 1b), often depicted undergoing a splitting in illustrations of the Rashba effect. However, it is crucial to note that at this stage, the bands of the 2DEG still remain spin-degenerate (also known as Kramers' degeneracy). This is understandable since the model Hamiltonian does not yet incorporate the SOI,

$$\hat{H}_{\mathrm{SOI}} = \frac{\hbar}{4{m_{\mathrm{e}}}^2c^2}(\nabla V \times \hat{\boldsymbol{p}})\cdot\boldsymbol{\sigma}, \tag{3}$$

where c is the speed of light, V is a potential, and σ represents the set of Pauli matrices $\boldsymbol{\sigma} = (\sigma_x,\sigma_y,\sigma_z)$. Nevertheless, even if the SOI is included, there is still no potential present in the system, meaning that $\hat{H}_{\mathrm{SOI}} = 0$. To address this, we will introduce such a potential as done in the BR model. Therefore, to facilitate inversion symmetry breaking (ISB), let's consider a 2DEG on a crystalline surface characterized by a surface potential V_{s} (see Fig. 1c). In this case, the potential leads to a non-zero electric field normal to the surface, given by $\nabla V_{\mathrm{s}} = (0,0,E_{\mathrm{s}})$. As the

Table 1 Glossary of key terms encountered in studies on spin splitting

Term	Definition
GSS	Giant spin splitting
Kramers' degeneracy	In a time-reversal symmetric system with half-integer total spin, for each energy eigenstate, there is at least one more eigenstate with the same energy
2DEG	Two-dimensional electron gas; it is a physical system employed in BR model
OAM	Orbital angular momentum of an electron
ISB	Inversion-symmetry breaking
Spin/SAM	Spin angular momentum of an electron
SOI/SOC	Spin–orbit interaction/spin–orbit coupling; a relativistic interaction of a particle's spin with its motion inside a potential
TRIM	Time-reversal-invariant momenta; it refer to high-symmetry points within the Brillouin zone that remain unchanged under the reversal of the system's time
BR/RB model	Bychkov–Rashba model; it describes the interaction of electron spins with an effective magnetic field arising from their relativistic motion in the presence of an electric field, leading to spin splitting
Orbital/OAM Rashba effect	An approach to the Rashba effect involving the separation of spin–orbit coupling and inversion symmetry breaking where The formation of an orbital angular momentum is the precursor to spin splitting

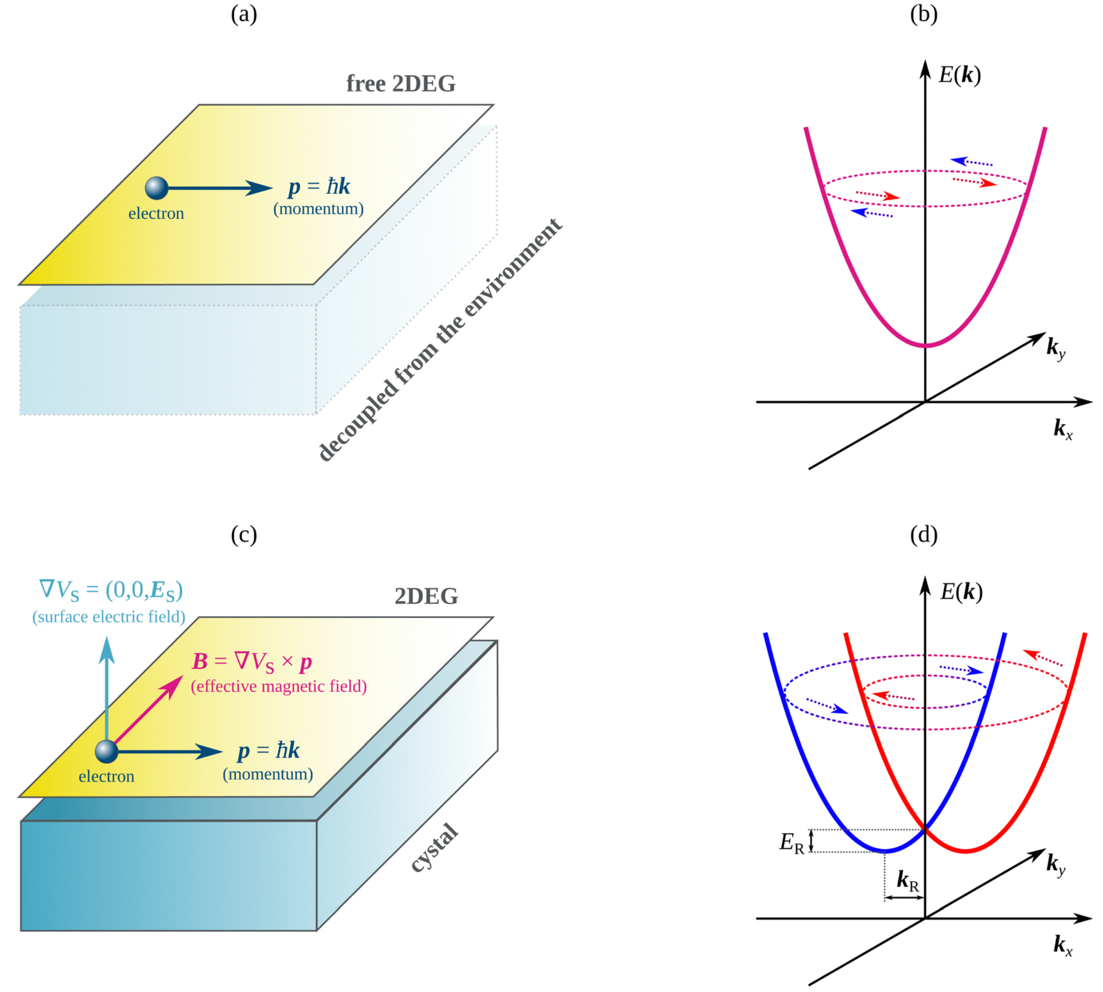

Fig. 1 (a) Schematic representation of 2DEG decoupled from structural asymmetry environment. (b) Spin-degenerated band of 2DEG without ISB. (c) Schematic depiction of 2DEG in presence of a surface potential leading to ISB. (d) Momentum-dependent splitting of spin bands governed by the BR model in presence of ISB.

electrons now move in this electric field, they experience an effective magnetic field, $\boldsymbol{B} = \nabla V_s \times \hat{\boldsymbol{p}}$, which couples with the electron spin by $\boldsymbol{B}{\cdot}\boldsymbol{\sigma}$. It should be also noted that since the electron momentum is parallel to the surface while the electric field is perpendicular, the effective magnetic field can only be parallel to it. As a consequence, the spin coupling can only occur for in-plane spin vectors, resulting in the so-called 'locking' of the electron's spin angular momentum and its linear momentum. Taken together, the SOI Rashba Hamiltonian takes the form of

$$\hat{H}_R = \alpha_R(\hat{z} \times \boldsymbol{k}_\parallel){\cdot}\boldsymbol{\sigma}_\parallel, \tag{4}$$

where $\boldsymbol{k}_\parallel = (k_x,k_y,0)$ is the in-plane wavevector, $\boldsymbol{\sigma}_\parallel = (\sigma_x,\sigma_y,0)$ is the in-plane spin, $\alpha_R = \dfrac{e\hbar^2 E_s}{4{m_e}^2c^2}$ is the Rashba parameter (also known as Rashba coupling). $\hat{H}_R$ is both spin- and momentum-depended, leading to a pair of split bands in the $\boldsymbol{k}$-space

$$E_{2\text{DEG+R}}(\boldsymbol{k}_\parallel) = \frac{\hbar^2 {\boldsymbol{k}_\parallel}^2}{2m_e} \pm \alpha_R|\boldsymbol{k}_\parallel|. \tag{5}$$

Consequently, within the RB model, the energy splitting between the parabolic bands is given by $E_R = 2\alpha_R|\boldsymbol{k}_\parallel|$, with $\boldsymbol{k}_R$ representing the offset by which the $E(\boldsymbol{k}_\parallel)$ parabolas are shifted away from the Γ point ($\boldsymbol{k}_\parallel = 0$). Additionally, this model results in complete spin polarization of the bands, such that the spin polarization vector in the surface plane exhibits an opposite direction for the two bands (see Fig. 1d). This leads to a chiral spin structure characterized by the ($\boldsymbol{\sigma}_x\boldsymbol{k}_y - \boldsymbol{\sigma}_y\boldsymbol{k}_x$) spin-momentum locking.

Before addressing the common limitations of the RB model, it is important to note that the preceding discussion serves as an introductory-level overview of the model. As a result, extensive derivation or overwhelming mathematical formalism has been intentionally avoided, with the focus primarily on the fundamental principles and central features of the model. Readers interested in a more formal derivation are encouraged to explore the model within the framework of $\boldsymbol{p}{\cdot}\boldsymbol{k}$ perturbation theory.[29] Additionally, it is worth mentioning that the crystal field does not significantly contribute to the Rashba effect in a manner that is relevant to understanding the model. Consequently, the discussion has omitted the crystal potential (V_{bulk}).

However, if included, the main difference would be the utilization of the effective mass m^*, and the split bands would be parabolic only in a local approximation.

3 Limitations of Bychkov–Rashba picture

The BR model qualitatively captures the effects observed experimentally, predicting both the spin splitting and the spin texture. However, despite its achievements, the model still presents several unresolved issues. First and foremost, the predicted energy scale of the band splitting is significantly underestimated for surfaces with GSS. The theoretical approximations of the Rashba coupling in the BR framework amount only to $\sim 10^{-3}$ meV Å, which would result in spin splitting much smaller than k_BT at room temperature. Nevertheless, the experimentally observed effects on surfaces of Au[25,30,31] or InSb[32] demand values on the order of ~ 100 meV Å, while in more extreme cases, such as Bi monolayers on Ag(001),[33] the parameter can even exceed 3 eV Å. Hence, the quantitative estimates of α_R from the BR model are orders of magnitude too small in the ideal 2DEG approach. In addition, GSS is known to favor high-atomic-number materials, which is not predicted by the BR model. For instance, α_R for Au(111) is ten times larger than for Ag(111),[34] despite comparable work functions between them, indicating that something is missing in this picture.

Several arguments have been proposed to address these issues. Notably, some researchers have highlighted the importance of the product of charge density (ρ) and the potential gradient along the surface normal ($\partial V/\partial z$) as a critical factor governing the magnitude of Rashba spin splitting[13,35]

$$\alpha_R \propto \int \rho(\boldsymbol{r})\frac{\partial V}{\partial z}\mathrm{d}\boldsymbol{r}. \tag{6}$$

This potential gradient is most prominent in the vicinity of the nuclei, making the charge density asymmetry along the z-direction near the nuclei the decisive factor for the splitting (see Fig. 2). Consequently, this approach involves investigating charge density profiles near surface atoms, wherein any asymmetric charge distribution is considered to explain the enhanced spin splitting.

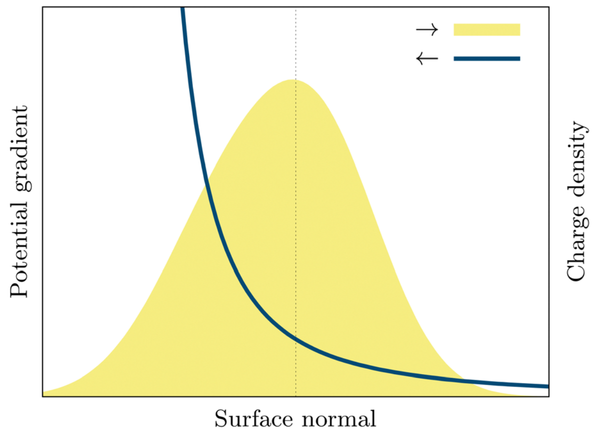

Fig. 2 Schematic graph for potential gradient (blue) and charge density (yellow) along surface normal. Dashed line indicates an nuclei position.

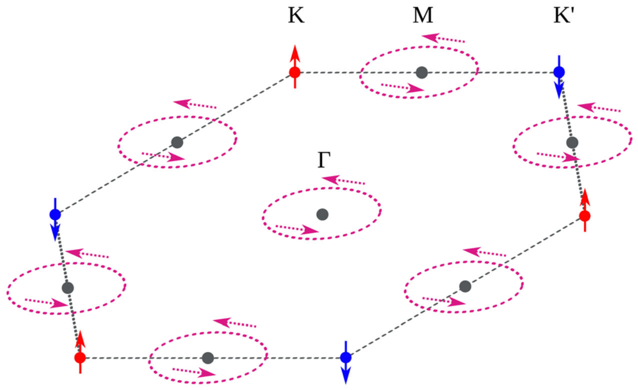

Fig. 3 Schematic illustration of the spin texture in k-space of some hexagonal system showing in-plane spin polarization around Γ and M points (fuchsia), and out-of plane polarization near K (red) and K' (blue).

On the other hand, some researchers argue that the splitting energy arises from the strong in-plane gradient of the crystal field in the surface layer.[28,36] Then, in cases with complex spin textures, others have explored the concept of the "*extended*" Rashba effect,[37,38] which can be represented as

$$\hat{H}_{eR} = \hat{H}_R + \boldsymbol{\sigma}\cdot\boldsymbol{B}_e(\boldsymbol{k}) \tag{7}$$

The second term is not considered in the case of an ideal 2DEG. However, in a *real* system, due to the 2D symmetry of the surface, an effective magnetic field $\boldsymbol{B}_e(\boldsymbol{k})$ can arise, leading to an abrupt rotation of spin at low symmetry points (see Fig. 3).

The above-mentioned arguments have proven helpful for certain systems. However, they remain somewhat speculative as they alone cannot fully explain all aspects of Rashba-related phenomena, nor do they support a quantitative analysis required for further validation. Consequently, the predictive power of the BR picture remains limited, even when expanded. The BR model, represented by eqn (4), significantly underestimates spin splitting when the effect is substantial, and it does not allow for spin splittings exceeding a few meV. Thus, it does not provide valuable insights to guide the search for materials with desirable GSS.

Eqn (6) emphasizes the importance of charge asymmetry. However, the asymmetry of charge is intrinsic to all surfaces, while its interplay with potential gradient is not intuitively obvious based solely on the material composition or structure. As a result, this approach is more suited to explain already observed spin splittings rather than guiding the discovery of superior materials for spintronics.

Lastly, the extended Rashba model, given by eqn (7), explores the role of the surface. Nonetheless, even if its impact is acknowledged, the relationship between the effective magnetic field and the material symmetry is not intuitive and proves rather challenging to assess both qualitatively and quantitatively.†

---

† $\boldsymbol{B}_e(\boldsymbol{k}) \approx \frac{\hbar^2}{4m_e^2c^2\Omega}\int \frac{1}{r}\frac{\mathrm{d}V(\boldsymbol{r})}{\mathrm{d}r}\left[u^*_{nk}(\boldsymbol{r}) \times \hat{L}u_{nk}(\boldsymbol{r})\right]\mathrm{d}\boldsymbol{r}$; see ref. 37 for details.

Consequently, the BR picture has not been the driving force behind material development. Instead, extensive experimental work has demonstrated which types of structures are capable of supporting GSS, with the BR model adjusted to fit the results.

4 What a chemist ought to do?

GSS was first observed on Au(111),[25] and subsequently on surfaces of other high-atomic-number materials, including Bi,[39] Gd,[40] and W.[41] Furthermore, when compared the results have demonstrated a relation between the atomic number of the comprising elements and the magnitude of the splitting. Notably, the surfaces of Bi, which is the heaviest of non-radioactive elements, exhibit spin splittings as large as 300 meV, while on Au it is only ∼100 meV. Consequently, these experimental studies have established that, apart from Rashba SOI, GSS is somehow affected by atomic SOI, which contrasts the ideal 2DEG picture. Further research has shown that Bi monolayers induce even greater spin splitting on surfaces of Ag, on the order of 1 eV.[28,33] Subsequently, similar effects have been reported for Tl, Pb, and Bi layers on semiconductor surfaces like Si(111)[36,37,42] and Ge(111).[13,43,44] Current research continues to explore the development of surface modifications.[45–50] However, it also delves into GSS induced in novel 2D layered materials, including transition-metal dichalcogenides (TMDs),[51–57] MXenes,[58–63] and a variety of other sheets.[64–72]

To facilitate the ongoing efforts, it is crucial to develop more robust strategies for enhancing spin splitting. Clear guiding principles need to be established to design materials with desired GSS. As a result, it becomes essential to thoroughly characterize and understand spin splitting in novel cases, such as on van der Waals (vdW) heterostructures,[3,52,54,60,64,73] topological insulators,[17,74,75] and Janus-type 2D materials.[61,63,70,72] Additionally, structural modification of these novel platforms must be considered to unlock their full potential for spintronics applications.

As such, it would seem that chemists could play a crucial role in the search for new materials for spintronics due to their expertise in understanding and manipulating the properties of materials at the atomic and molecular levels. The chemical perspective could be particularly insightful in:

- Materials synthesis: chemists are skilled in designing and synthesizing various materials with specific properties. In spintronics, they can create new compounds or modify existing materials to optimize their electronic and magnetic properties, making them suitable for spintronic applications.
- Thin-film deposition techniques: spintronic devices frequently utilize thin films of materials with customized properties, and the understanding of chemical principles is pivotal in the effective use of dedicated techniques like chemical vapor deposition (CVD) or atomic layer deposition (ALD).
- Materials design and tailoring: by understanding the principles of chemical bonding and electronic structure, chemists can design and tailor materials with specific properties relevant to spintronics, such as strong spin–orbit coupling, long spin relaxation times, and high spin polarization.
- Quantum chemistry and computational modeling: chemists can use quantum chemistry calculations and computational modeling to predict the electronic and magnetic properties of materials. These techniques help in screening large databases of materials to identify promising candidates for spintronic applications.

However, what about a comprehensive characterization and deep insight into the mechanisms responsible for the arising spin splitting? Even if it occurs in new materials, without a well-described mechanism behind the splitting, the potential for developing more robust strategies for enhancing spin splitting will be limited despite the clear need for guiding principles in GSS engineering. Unfortunately, this is the aspect where many chemically-oriented investigations fall short.

In such cases, researchers often resort to using the BR picture to describe the effects of structural modification. Consequently, they fail to recognize the role of atomic SOI. Instead, the observed GSS is interpreted within the framework of a 2DEG model in accordance with eqn (4). However, since this approach cannot predict the energy scale of the band splitting, the model is usually supplemented with experimental or computational data to fit the model, *i.e.*,

$$\alpha_{\mathrm{R}} = \frac{2E(\text{expt./calc.})}{k_{\mathrm{R}}}. \tag{8}$$

Unfortunately, this approach splits the Rashba coupling from its theoretical framework, making it challenging to reasonably explain why certain chemical modifications induce desired effects while others do not, especially since work functions themselves were shown insufficient to explain variation in GSS.

While still working in the BR framework, researchers could consider some of the proposed amendments. Consequently, the role of the interplay between charge density and the potential gradient along the surface normal could be highlighted. Still, it should be noted that Nagano *et al.*[35] formulated the relation, given by eqn (6), for surface systems where broken bonding configuration results in asymmetric features of the surface state in the nucleus region, *i.e.*, within one Bohr around the surface atom. Hence, when employed for the vdW interface, the argumentation should be used with care. Interestingly, both Nagano *et al.*[35] and Sakamoto *et al.*[37] have simultaneously discussed the abrupt rotation of the spin vector within the BR picture, emphasizing the role of the 2D hexagonal system of the surfaces on which it occurs. Hence, a similar approach could be adopted for modified TMDs as well as other p3m1 and p31m layers. Nevertheless, such argumentation may prove difficult, since it was shown that GSS for hexagonal systems can be enhanced or quenched for the same surfaces and adsorption layers depending only on the adsorption site of the latter.[38,76]

Hence, what can a chemist do in this situation? The BR framework is frequently used in material investigations, but it poses challenges when trying to account for the effects of chemical engineering. Additionally, it provides no guidance in the selection of structures and modifications. As a result,

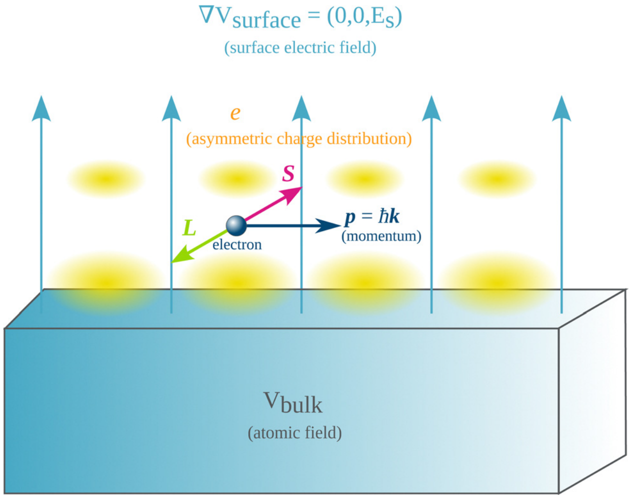

Fig. 4 Schematic of the model system in the orbital picture of the spin splitting of surface bands. Electron (blue) has non-zero spin (fuchsia) and orbital angular momentum (lime) while moving in the presence of crystal and surface potentials.

many researchers find themselves without the necessary tools to address the problems at hand and meaningfully contribute to the search for optimal materials for spintronic applications.

However, there exists an elegant and approachable solution to most of the highlighted problems. That is, to recognize the role of atomic SOI in the formation of GSS, and adopt the so-called orbital Rashba picture,[77,78] where local orbital angular momentum (OAM) plays a crucial role in the effect. The rise of unquenched OAM *via* chemical functionalization can be easily understood, explored, and exploited. Therefore, it could be an optimal tool for chemists to investigate materials with GSS.

5 Orbital Rashba picture

To address the aforementioned limitations and gain a clear understanding of the orbital Rashba picture, let us consider an effective Hamiltonian of a bulk system, which includes three terms:

$$\hat{H} = \frac{\hat{\boldsymbol{p}}^2}{2m_\mathrm{e}} + V + \frac{\hbar}{4{m_\mathrm{e}}^2c^2}(\nabla V \times \hat{\boldsymbol{p}})\cdot\boldsymbol{\sigma}. \qquad (9)$$

Next, we will break the symmetry of the crystal field by introducing a surface (see Fig. 4). In the presence of ISB, we need to consider an extra electric potential in addition to the atomic field. Let's assume that this external potential has only a z component, and thus, we replace V with $V_\mathrm{bulk} + V_\mathrm{surface}$, where V_surface can be approximated as $E_\mathrm{s}z$. Under these conditions, the expression for eqn (9) takes on the form

$$\begin{aligned}\hat{H} &= \frac{\hat{\boldsymbol{p}}^2}{2m_\mathrm{e}} + V_\mathrm{bulk} + \frac{\hbar}{4{m_\mathrm{e}}^2c^2}(\nabla V_\mathrm{bulk} \times \hat{\boldsymbol{p}})\cdot\boldsymbol{\sigma} \\ &\quad + \frac{e\hbar E_\mathrm{s}}{4{m_\mathrm{e}}^2c^2}(\nabla\hat{z} \times \hat{\boldsymbol{p}})\cdot\boldsymbol{\sigma} + eE_\mathrm{s}z\end{aligned} \qquad (10)$$

The first two terms, representing the kinetic and potential energies in the bulk, give rise to the usual band energy. The third term describes the atomic SOI and can be expressed as:

$$\hat{H}_\mathrm{SOI} = \xi\hat{\boldsymbol{L}}\cdot\hat{\boldsymbol{S}}, \qquad (11)$$

where ξ is the coupling constant, while $\hat{\boldsymbol{L}}$ and $\hat{\boldsymbol{S}}$ are the angular momentum and spin angular momentum operators, respectively. The fourth term is the Rashba Hamiltonian, $\hat{H}_\mathrm{R}$, as given in eqn (3) and (4). Finally, the fifth term accounts for the interaction between the asymmetric charge distribution and the surface electrostatic field, which can be approximately expressed as:[78–80]

$$\hat{H}_\mathrm{Es} = \hat{\boldsymbol{p}}\cdot\boldsymbol{E}_\mathrm{s} = \beta(\boldsymbol{k} \times \boldsymbol{E}_\mathrm{s})\cdot\hat{\boldsymbol{L}}, \qquad (12)$$

where β is a proportionality constant dependent on the overlap of atomic orbitals.[79] However, it should be noted that, this description of the electrostatic energy remains valid when $\boldsymbol{k}$ is sufficiently close to any time-reversal-invariant momentum (TRIM) points.[78]

In this system, three terms from eqn (10) could potentially contribute to lifting spin degeneracy: $\hat{H}_\mathrm{R}$, $\hat{H}_\mathrm{SOI}$, and $\hat{H}_\mathrm{Es}$. The influence of the Rashba SOI, as mentioned earlier, is generally negligible, leading to energy splittings of only a few meV. Conversely, atomic SOI for high-atomic-number elements can easily be on the order of 1 eV. Similarly, the electrostatic Hamiltonian can also facilitate the experimentally observed energy splitting scale, as $\boldsymbol{p}\cdot\boldsymbol{E}_\mathrm{s} \sim e\text{Å} \times \text{V/Å} \sim \text{eV}$.[78–80] Therefore, both new terms may contribute to the generation of GSS in the presence of non-vanishing OAM.

Box 1 Atomic orbitals and quantum numbers

Atomic orbitals refer to one-electron wavefunctions that serve as quantum-mechanical solutions to the Schrödinger equation. They give distinct atomic energy levels for electrons to occupy, and they can be intuitively understood as electron clouds. Each orbital in an atom is characterized by a set of values, resulting in distinct electronic states. The principal quantum number (n) designates the main energy level of an atomic orbital, dictating its size and distance from the nucleus. The orbital (azimuthal) quantum number (l) delineates the orbital angular momentum and shape, resulting in different types of orbitals such as s, p, d, and f orbitals. The magnetic quantum number (m_l) specifies the orientation of an orbital within a given energy level and shape, enabling differentiation of individual orbitals of the same type. The spin quantum number (m_s) indicates the intrinsic spin of an electron within an orbital, highlighting its fundamental quantum property.

As a result, the orbital picture attributes the band splitting to the rise of unfurnished OAM *via* atomic SOI and the interaction between the electrostatic field due to ISB and the asymmetric charge distribution. However, which term is dominant depends on the material, with those having strong SOI, such as Au(111), experiencing spin degeneracy predominantly lifted by $\hat{H}_\mathrm{SOI}$

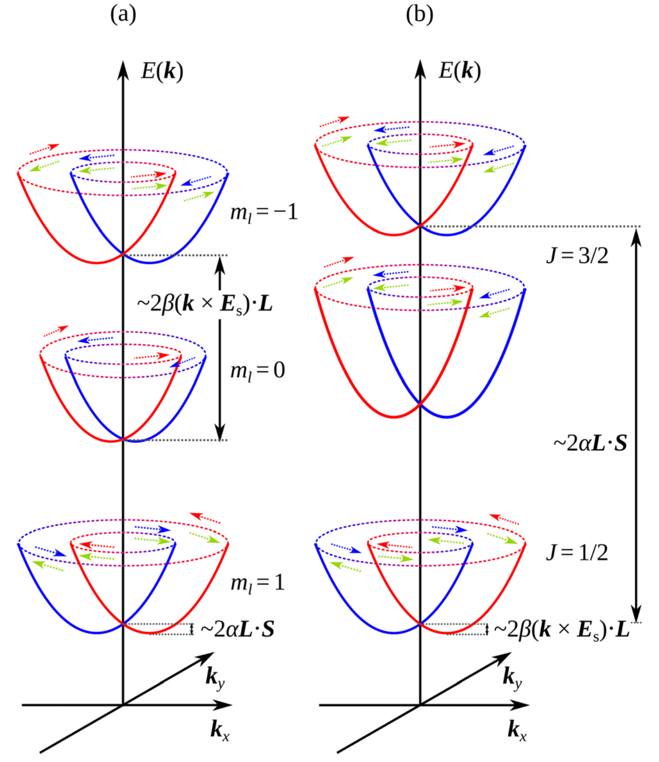

Fig. 5 Schematic of energy levels with Rashba-type splitting for p states in the case of (a) strong and (b) very strong SOI. Red and blue arrows symbolize spin, while lime-colored arrows represent OAM.

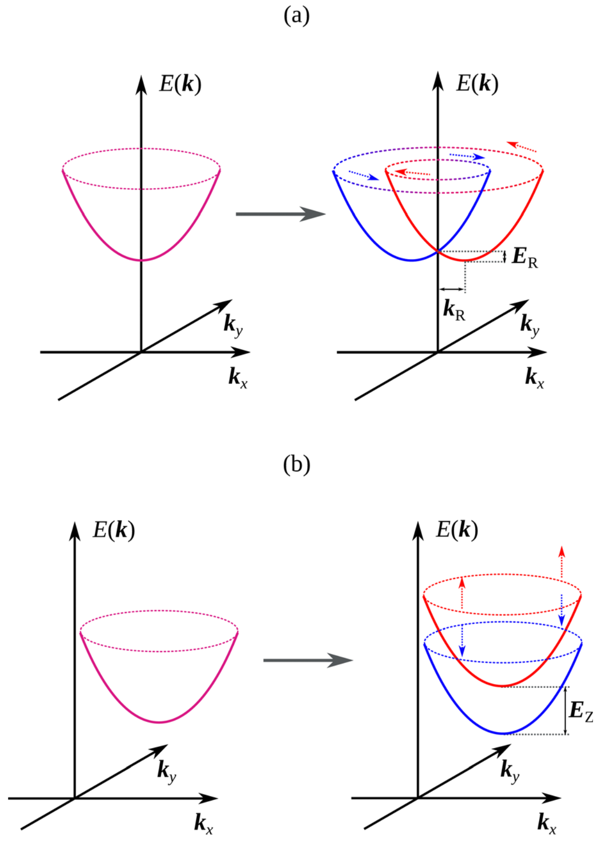

Fig. 6 Schematic depiction of the band structure and spin-texture of systems featuring the (a) Rashba and (b) Zeeman effects. The red and blue arrows indicate the orientation of spin polarization.

(see Fig. 5a), while those with very strong coupling, like Bi_2Te_2Se, exhibiting splitting dominated by $\hat{H}_{Es}$ (see Fig. 5b). Furthermore, as $\boldsymbol{k}$ is confined to the surface plane while $\boldsymbol{E}_s$ is normal to it, $\hat{H}_{Es}$ naturally couples in-plane OAM, resulting in a Rashba-type spin splitting. This leads to lifting the degeneracy by offsetting the bands in the momentum space around a TRIM point and complete spin polarization of the bands, with the spin polarization vectors exhibiting opposite directions for the two bands (see Fig. 6a). On the other hand, $\hat{H}_{SOI}$ can couple both in-plane and out-of-plane spin. Consequently, it can also facilitate a Zeeman-type splitting ($\boldsymbol{L}\cdot\boldsymbol{S} \sim \sigma\cdot\boldsymbol{B}_{SOI}$), where at a low-symmetry point bands are shifted on the energy scale depending on the spin polarization (see Fig. 6b).

Taken together, it is clear that optimizing GSS requires a keen understanding of the interplay between the atomic SOI, locking the SAM on the OAM direction, and the crystal field, which lifts the degeneracy of the OAM. That being said, it becomes imperative to delve into the mechanisms driving the emergence of non-vanishing orbital momentum in surface systems. Furthermore, we should explore the intricate connection between this phenomenon and the underlying chemical structure of materials.

6 Non-vanishing orbital momentum

Before delving into the intricacies of non-zero OAM in crystal structures, it's essential to first examine the behavior of OAM within isolated atoms and understand how it becomes suppressed within bulk materials. In free atoms, the OAM of electrons is well-defined and able to contribute significantly to the total angular momentum of the atom. Its non-zero values arise from the spherical potential generated by the atomic nuclei, *i.e.*, $V_{atom} \sim 1/r$, since the symmetry of this potential leads to constant values for the square of the OAM, as well as for one of its components (often represented as L_z), *i.e.*,

$$L^2, L_z = \text{const.} \tag{13}$$

Hence, given the well-known characteristics of atomic orbitals (described in Box 1), we can express the relation between the magnitude of OAM and the orbital quantum number

$$L^2 = \hbar^2\, l(l+1), \tag{14}$$

while the projection of the orbital angular momentum along a specified axis we can quantified by using the magnetic quantum number of specific orbital

$$L_z = m_l\hbar. \tag{15}$$

However, it's crucial to bear in mind that the eqn (14) and (13) have been derived for central fields. Consequently, their applicability is not universal and they lose validity when confronted with symmetry-breaking situations. In the presence of a non-central field the constancy of the OAM components becomes

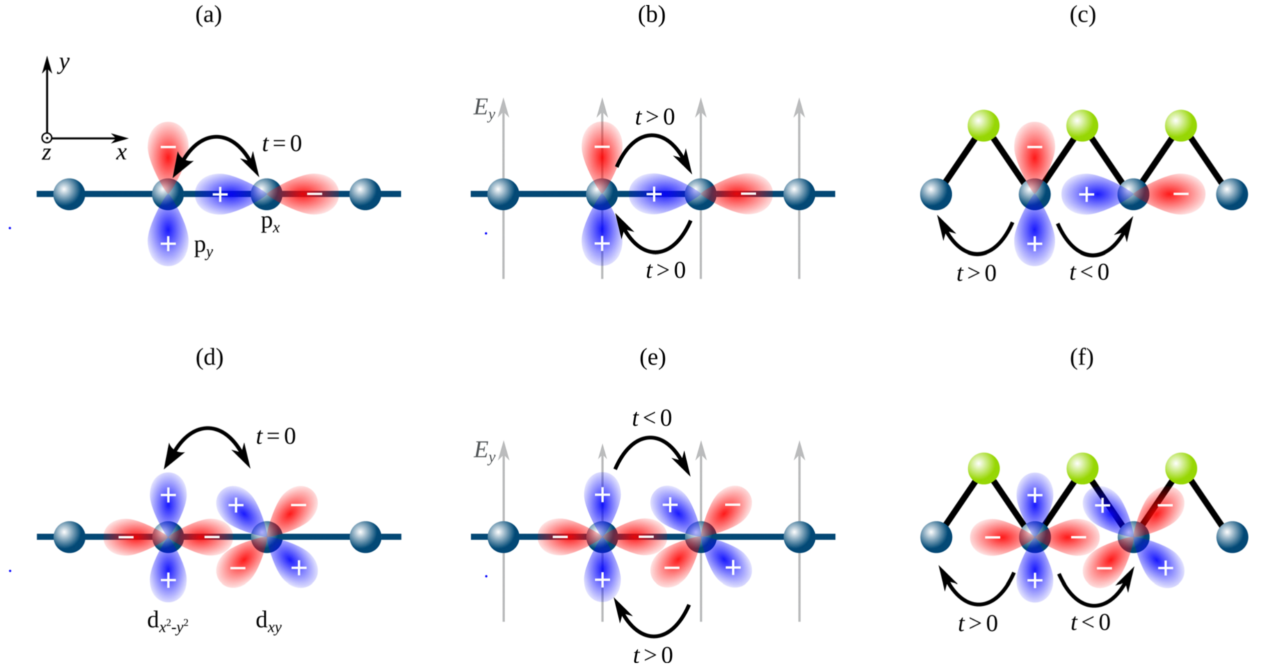

Fig. 7 Symmetry breaking in an atomic chain giving rise to k-antisymmetric orbital momentum; (a) and (d) no ISB, (b) and (e) electrostatic symmetry breaking, and (c) and (f) geometric symmetry breaking. (a)–(c) Atomic sites comprising p_x and p_y orbitals. (d) and (f) Atomic sites comprising $\mathrm{d}_{x^2-y^2}$ and d_{xy} orbitals. In panels (a) and (d), interatomic hopping energy between orbitals is zero owing to the presence of a mirror plane parallel to the xz plane. In panels (c), (c), (e), and (f), there is no mirror plane parallel to the xz plane, resulting in non-zero interatomic hopping between orbitals of differing parity.

compromised, potentially resulting in an averaging out to zero. This phenomenon is particularly evident in crystals where the OAM tends to be suppressed. This occurs due to the facilitation of wavefunction mixing by the crystal's field, leading to the creation of electronic states characterized by an effective OAM close to zero. Consequently, in the context of most bulk materials, the magnetic properties are predominantly attributed to spin, rather than the overall angular momentum, precisely due to this effect.

So, how can we induce non-vanishing OAM within crystals? The short answer is: by mixing orthogonal orbitals, such that the hybrid is antisymmetric in momentum space.[76–78] However, to delve deeper into this concept, let's once again consider a fictitious system. In Fig. 7a, an atomic chain is aligned along the x-axis, with each atomic site comprising p_x and p_y orbitals. Due to the chain's mirror symmetry plane running parallel to the xz plane, the p_x and p_y orbitals remain orthogonal to each other and decoupled,

$$\langle \mathrm{p}_x|\hat{H}|\mathrm{p}_y\rangle = \langle \mathrm{p}_y|\hat{H}|\mathrm{p}_x\rangle = 0. \tag{16}$$

As a consequence, the orbitals give rise to two bands characterized by zero OAM

$$\langle \mathrm{p}_x|\hat{\boldsymbol{L}}|\mathrm{p}_y\rangle = \langle \mathrm{p}_y|\hat{\boldsymbol{L}}|\mathrm{p}_x\rangle = 0. \tag{17}$$

However, if we introduce a perturbation that disrupts the xz symmetry plane, such as by applying an external field along the y-axis (as depicted in Fig. 7b) or through the presence of neighboring atoms (as illustrated in Fig. 7c), the initially uncoupled p_x and p_y orbitals will mix. This interaction aims to minimize the overall energy of the system, leading to the emergence of a non-zero nearest-neighbor hopping energy t

$$\langle \mathrm{p}_x|\hat{H}|\mathrm{p}_y\rangle = -2it_{\mathrm{p}_x\mathrm{p}_y}\sin(ka), \tag{18}$$

where a the lattice constant.[81] This effect facilitates the formation of bands exhibiting non-zero OAM,[82] characterized by the expectation value $\boldsymbol{L} = \langle\hat{\boldsymbol{L}}\rangle = \langle p_i|\hat{\boldsymbol{L}}|p_j\rangle$. Therefore, for the chosen geometry, the values of OAM at each atomic site will give

$$\langle\hat{\boldsymbol{L}}_x\rangle = \langle\hat{\boldsymbol{L}}_y\rangle = 0, \tag{19}$$

$$\langle\hat{\boldsymbol{L}}_z\rangle \sim t_{\mathrm{p}_x\mathrm{p}_y}\sin(ka). \tag{20}$$

Furthermore, due to the different parities of the orbitals relative to the xz plane‡, the hopping energy from p_x to y along the x direction carries an opposing sign to that in the $-x$ direction. Therefore, the resulting OAM will be k-antisymmetric

$$\boldsymbol{L}(k) = -\boldsymbol{L}(-k). \tag{21}$$

The very same mechanism applies seamlessly when transitioning from p-type to d-type orbitals. In the case of an atomic chain aligned along the x-axis with each atomic site comprising $\mathrm{d}_{x^2-y^2}$ and d_{xy} orbitals (see Fig. 7d), the orbitals will be decoupled from each other, and they will form two bands with zero OAM. However, if this symmetry plane is broken (see Fig. 7e and f), the orbitals will become coupled, and $\langle\hat{\boldsymbol{L}}_z\rangle$ will

---

‡ Parity, also known as inversion, indicates whether an orbital exhibits symmetry or antisymmetry when subjected to an inversion operation.

be proportional to the interatomic hopping energy between d$_{x^2-y^2}$ and d$_{xy}$.

Naturally, these model examples are simple, providing only a glimpse into the myriad scenarios for inducing non-vanishing OAM. GSS has been observed in a wide range of materials. Hence, it would be prudent to delve into a selection of real examples. This endeavor will provide a more nuanced perspective, demonstrating how the aforementioned methodology can be applied effectively in practical situations.

7 Examples

In order to address a diverse range of relevant scenarios, this section examines GSS formation using real-world materials, including Au(111), Pb/Si(111)-1 × 1, MoS$_2$, HgTe, and GaAs. These examples embody distinct material classes featuring GSS: a high-atomic-number metal surface, a semiconductor surface decorated with high-atomic-number elements, and a 2D sheet. Each of these selected materials holds significance in spintronics and presents a characteristic case of GSS formation that is representative of a specific class of structures.

7.1 Au(111)

First, let's delve into the well-known Rashba-type splitting of Au(111), utilizing the orbital framework to elucidate the formation of the GSS. The surface states in this material encompass 6s, 6p, and 5d orbitals. At the Γ point, where symmetry dictates zero OAM and spin splitting, the states comprise decoupled s, p$_z$, and d$_{z^2}$ orbitals. However, as we move from this high-symmetry point, surface effects come into play, leading to momentum-dependent intra-atomic orbital coupling. This interplay along the $\boldsymbol{k}_x$ direction gives rise to mixing between p$_z$/p$_x$ and d$_{z^2}$/d$_{xz}$ orbitals. Conversely, coupling along $\boldsymbol{k}_y$ involves p$_z$/p$_y$ and d$_{z^2}$/d$_{yz}$ orbitals, resulting in intermediate mixing at wavevectors in between. The differing parity of these coupled orbitals facilitates non-zero interatomic hopping energies between p$_z$ and p$_x$ (p$_y$) orbitals (Fig. 8a), as well as between d$_{z^2}$ and d$_x$ (d$_{yz}$) orbitals (Fig. 8b).

As we now know, the non-zero hopping energy gives rise to bands possessing non-zero OAM. Moreover, due to the momentum-dependent mixing, these interorbital hoppings induce a non-zero $\langle \hat{L}_y \rangle$ along $\boldsymbol{k}_x$, and $\langle \hat{L}_x \rangle$ along $\boldsymbol{k}_y$. Consequently, a chiral OAM structure emerges around the Γ point (depicted in Fig. 8c). This chiral OAM couples with a spin *via* atomic SOI, causing the spin to adopt in-plane polarization and circulate within momentum space around Γ (illustrated in Fig. 8d). In terms of the splitting magnitude, it is worth noting that the atomic SOI strength of the 6p orbitals is considerably smaller than that of the 5d orbitals in Au. Hence, the 5d orbitals will have a significant contribution to GSS. However, the splitting will not reach the same magnitude as the atomic SOI for 5d orbitals in Au, due to the surface states not being exclusively composed of 5d orbitals.

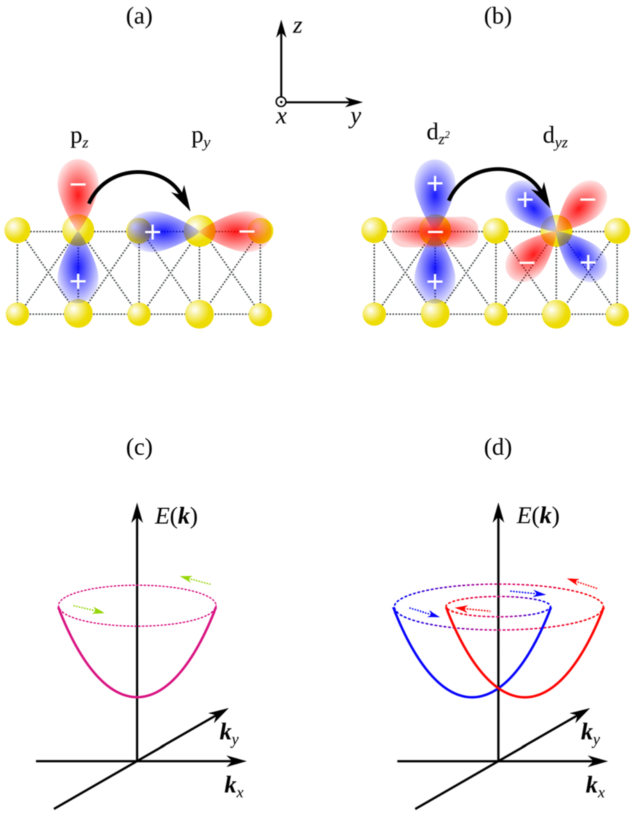

Fig. 8 Au(111) surface. Panels (a) and (b) illustrations depicting the interatomic hopping interactions between (a) p$_z$ and p$_y$ orbitals, as well as (b) d$_{z^2}$ and d$_{xy}$ orbitals of the outermost layer of Au atoms on the surface. (c) Shows spin degenerated surface bands near Γ in the absence of SOI, with a notable chiral texture characterized by lime-colored arrows. (d) Illustrates the impact of SOI on the surface bands near the Γ point, showcasing Rashba-type splitting (blue and red colors indicate spin polarization).

The described mechanisms driving GSS formation remain applicable to various other transition metals, albeit with some variation. In practical terms, the same fundamental principles underpinning the emergence of unquenched OAM are observed in Cu(111) and Ag(111), owing to the shared face-centered cubic (FCC) crystal structure and their membership in group 11. Nevertheless, due to substantial variations in their atomic SOI, only the surface of gold will exhibit GSS. In other cases, distinct crystal structures and electronic configurations of elements will yield diverse band structures, but still, a similar interplay between orbitals will govern the Rashba-type splitting on pristine surfaces of d-block elements.

7.2 Pb/Si(111)-1 × 1

Now, let's delve into the influence of surface bonding on GSS formation, which should hold particular relevance for chemists or individuals aiming to utilize chemical modifications of surfaces to facilitate GSS. To explore this, we will examine the intriguing case of Pb/Si(111)-1 × 1. In this structure, GSS at the K-point of its surface Brillouin zone can either be suppressed or enhanced, depending upon the specific adsorption site of Pb atoms.

Silicon possesses a face-centered diamond-cubic crystal structure. Hence, when cleaved along the (111) plane, the

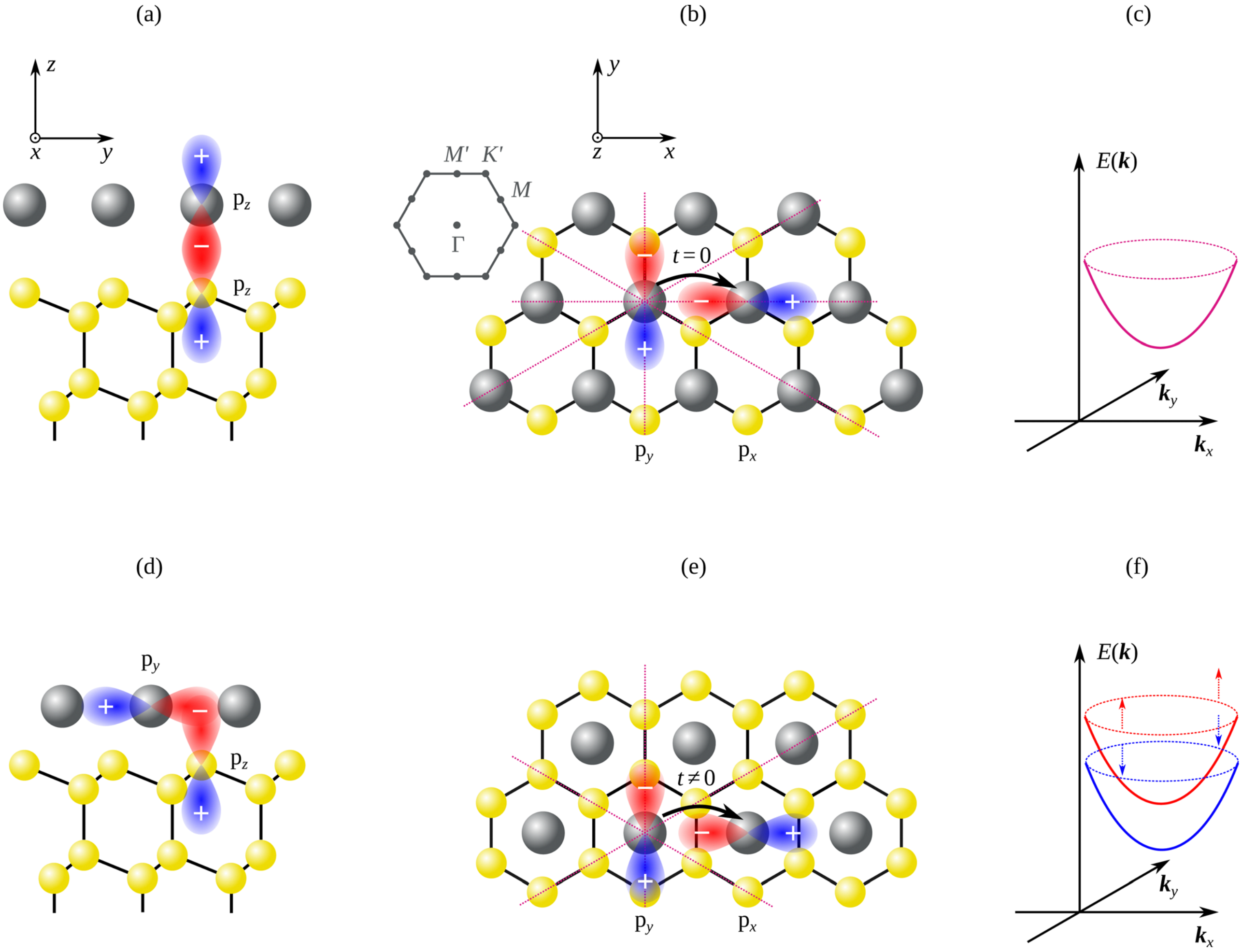

Fig. 9 Pb/Si(111)-1 × 1 surface configurations and electronic bands. Panels (a) and (b) Showcase side and top views of the T_1 configuration, where Pb atoms reside above the topmost Si atoms. (c) Depicts the surface bands in the T_1 configuration, featuring the p_x and p_y orbitals of Pb near the K-point. Notably, despite the substantial atomic SOI of Pb, the bands remain spin-degenerate, with predominantly in-plane orientation of the spin vector (there is no circular rotation of spin around K as it is not a TRIM point). (d) and (e) Present side and top views of the H_3 configuration, with Pb atoms positioned above the fourth-layer Si atoms. (f) Illustrates the surface bands in the H_3 configuration, again involving the p_x and p_y orbitals of Pb near the K point. Changing the adsorption site results in an abrupt rotation of the spin vector and a GSS of ≈800 meV. Panels (a) and (d) include a schematic representation of the Pb–Si bonding hybridization, while panels (b) and (e) highlight the p_x and p_y orbitals of Pb contributing to bonding in the adsorption layer, along with the mirror symmetry planes of the in-plane Pb hybrids (dashed lines).

resultant surface—assuming the absence of reconstruction (*i.e.*, a 1 × 1 cell)—exhibits atoms arranged in a hexagonal symmetry. Within this arrangement, each double layer of silicon forms a buckled honeycomb structure, which is stacked with an AB–BC–CA sequence along the surface's normal direction. This stacking gives rise to three distinct adsorption sites within the 1 × 1 cell: T_1, T_4, and H_3. These sites correspond to atoms adsorbed on top of the topmost, second, and fourth layer of silicon atoms, respectively. When Pb is adsorbed at site T_1, it leads to a quenched spin splitting at the K-point. On the other hand, adsorption at sites T_4, and H_3 results in a GSS of ≈800 meV.[38] As a result, for our discussion, we will focus on the T_1 configuration (see Fig. 9a and b) and the H_3 configuration (see Fig. 9d and e).

At first glance, the disparity in spin splitting between these configurations might appear puzzling, considering they occur on the same surface, decorated with the same elements arranged in identical patterns. Consequently, we are confronted with cases involving comparable surface potentials and identical atomic SOI. This, in itself, could pose a challenge when attempting to reconcile within the framework of the original Rashba model. However, given our understanding that orbital hybridization of surface states leads to non-vanishing OAM, it is reasonable to suspect that surface bonds affect the splitting depending on the orbitals they mix.

Upon closer examination, it becomes apparent that the bonding between Pb and Si in the T_1 configuration involves the p_z orbitals of both Pb and Si (see Fig. 9a). This leaves the p_x–p_y hybrids in the Pb layers mostly unaffected, effectively decoupling them from the structural asymmetry of the environment. As a result, despite the three-fold symmetry of the Si substrate, the six-fold symmetry of the p_x–p_y states of Pb remains intact.

This, in turn, allows the monolayer to maintain mirror symmetry in the *xz* plane, preserving the relative parity of the p_x–p_y orbitals (see Fig. 9b). Consequently, the interatomic hopping energy between these orbitals along the *x* direction approximates zero. As a result, the p_x and p_y orbitals do not contribute to a non-zero $\langle \hat{L}_z \rangle$ along the Γ–K path, leading to the absence of GSS at the *K* point (depicted in Fig. 9c).

In contrast, the bonding between Pb and Si in the H_3 configuration once again involves the p_z orbitals of Si, but this time, it includes the p_x and p_y orbitals of Pb (see Fig. 9d). This effectively breaks the six-fold symmetry within the p_x–p_y hybrids in the Pb layer, resulting in their loss of mirror symmetry in the *xz* plane (see Fig. 9e). Consequently, as these orbitals exhibit different parities with respect to the *xz* plane, the interatomic hopping energy between the p_x and p_y orbitals along the *x* direction assumes a non-zero value. This, in turn, gives rise to an unquenched $\langle \hat{L}_z \rangle$ along the Γ–K path, which couples spin *via* $\boldsymbol{L}\cdot\boldsymbol{S}$, facilitating Zeeman-type splitting centered at the *K* point (shown in Fig. 9f). Given that the bands predominantly comprise Pb 6p orbitals, which are characterized by strong atomic SOI, this results in a significant GSS of $\approx$0.8 eV. Also, it is noteworthy that, since the hopping energy from p_x to p_y along the *x* direction carries an opposing sign compared to that in the $-x$ direction, the polarization of spin is opposite between the *K* and K' points.

The outlined mechanisms driving the formation of GSS can be considered as somewhat characteristic of p3m1 surfaces with decorations comprising high-atomic-number elements from the p-block. This is rooted in the fact that all p_x–p_z and p_y–p_z bonds disrupt the inherent six-fold symmetry of in-plane hybrids regardless of the elements comprising the surface. Consequently, if such bonds are formed, the resulting loss of symmetry enables p_x–p_y coupling to generate non-vanishing $\langle \hat{L}_z \rangle$, with the extent of splitting predominantly contingent on the atomic SOI of the adsorbate. Consequently, this relationship between symmetry, surface bonding, and SOI has facilitated the same type of GSS in materials such as Tl/Si(111)-1 × 1,[37] Pb/Ge(111)-1 × 1,[76] Pb/germanene,[65] and X/silicene (X = Tl, Pb, Bi).[66]

7.3 MoS_2

Turning to our next example, let's shift our focus to the class of 2D layered materials, an area that has recently garnered significant attention within spintronics research.[73,83–86] In this context, we will delve into hexagonal-phase transition-metal dichalcogenides (TMDs), which have piqued interest due to their novel properties. Notably, these materials stand out as semiconductors featuring GSS at the top of their valence band.[87–91] Prominent examples of such TMDs encompass molybdenum disulfide (MoS_2), molybdenum diselenide ($MoSe_2$), molybdenum ditelluride ($MoTe_2$), tungsten disulfide (WS_2), and tungsten diselenide (WSe_2). For our current purpose, we will focus on MoS_2, given its status as one of the most extensively studied TMD sheets. Nevertheless, it is crucial to acknowledge that the same underlying mechanisms govern GSS within the other monolayers of this group. The MoS_2 monolayer consists of three atomic layers, with a central layer of Mo sandwiched between two layers of S. Within the monolayer, Mo atoms favor sd^5 hybridization, yielding a trigonal-prismatic bonding geometry. This arrangement imparts mirror symmetry to MoS_2 monolayers at the plane containing Mo atoms—let's denote it as the *xy* plane (refer to Fig. 10a). Consequently, both $\langle \hat{L}_x \rangle$ and $\langle \hat{L}_y \rangle$ remain quenched, thereby precluding the formation of Rashba-type splitting around the Γ point despite the presence of the surface.

Nonetheless, a Zeeman-type splitting does manifest at the *K* and K' points, a phenomenon attributed to the lack of in-plane symmetry. To grasp this concept more comprehensively, let's inspect the structure of MoS_2 in more detail. Upon examining the monolayer from a top-down perspective, an additional mirror plane emerges parallel to the *yz* plane (see Fig. 10b). Consequently, along the Γ–M line, $\langle \hat{L}_z \rangle$ equates to zero, thus preventing any occurrence of spin splitting. However, as we move away from this line and explore $\boldsymbol{k}$ vectors that deviate from it, the absence of additional mirror symmetry becomes evident, allowing for $\langle \hat{L}_z \rangle$ to exhibit non-zero values.

The split states at the valence band maximum are predominantly composed of d_{xy} and $d_{x^2-y^2}$ orbitals of Mo. Therefore, when we investigate the valence-band states with $\boldsymbol{k}$ directed along the Γ–K path in the $\boldsymbol{k}_x$ direction, it becomes evident that $\langle \hat{L}_z \rangle$ will be directly proportional to the interatomic hopping energy between these orbitals along the *x* direction, which is non-zero due to the presence of S ions. Subsequently, the non-zero OAM couples with spin *via* the strong atomic SOI of Mo's 4d orbitals, resulting in splitting governed by $\boldsymbol{L}\cdot\boldsymbol{S}$, and spin polarization along the *z* direction (see Fig. 10c). Notably, these features of GSS concur with computational predictions and experimental findings for TMDs.[51–57] Furthermore, owing to the distinct parities of these orbitals relative to the *yz* plane, the hopping energy from d_{xy} to $d_{x^2-y^2}$ along the *x* direction carries an opposing sign to that in the $-x$ direction. Thus, as a natural consequence, the observed splitting along the Γ–K' path exhibits reverse spin polarization—a characteristic feature inherent to hexagonal structures.

In the pursuit of material functionalization, it is important to recognize that Rashba-type splitting can also be induced in TMDs. Achieving this necessitates breaking the inherent *xy* mirror symmetry of the monolayer. This can be achieved through various means, such as applying an external electric field (depicted in Fig. 10d), adsorbing high-atomic-number elements (as illustrated in Fig. 10e), or utilizing Janus TMD—monolayers composed of a transition metal layer sandwiched between two distinct chalcogen atomic layers, for example, MoSSe (see Fig. 10f). In such cases, the absence of *xy* symmetry permits non-zero values for $\langle \hat{L}_x \rangle$ and $\langle \hat{L}_y \rangle$, which can have a significant impact on the GSS. In particular, electronic states of the highest valence band near the Γ point are known to be notably affected. With the *xy* symmetry intact, the band consists mostly of d_{z^2} orbitals of Mo. However, in the presence of ISB, d_{z^2} orbitals couple with d_{xz} along the $\boldsymbol{k}_x$ direction and with d_{yz} along the $\boldsymbol{k}_y$ direction. Notably, due to the distinct parity of the coupled orbitals in relation to the *xy*

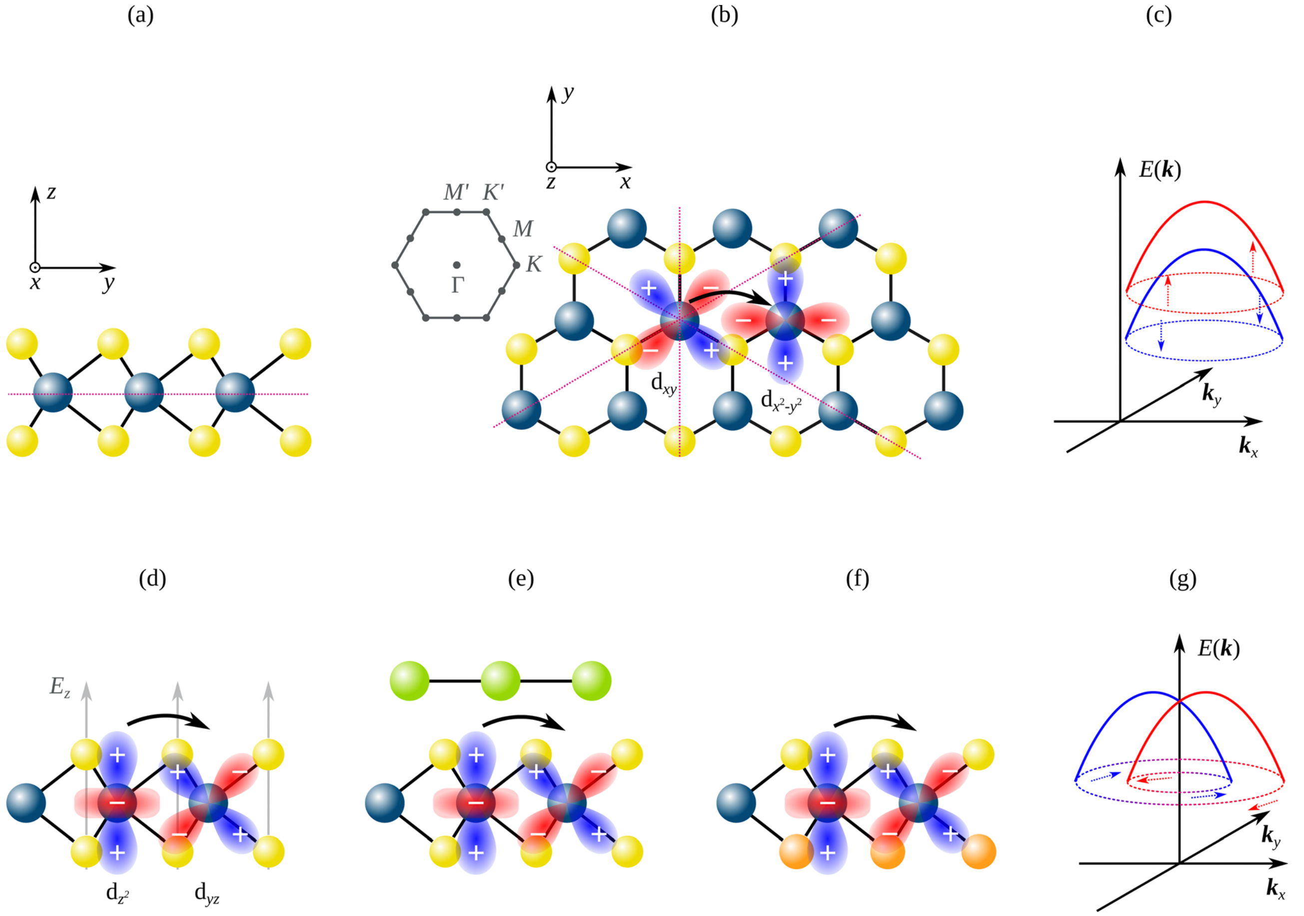

Fig. 10 MoS$_2$ structure and electronic bands. Panel (a) illustrates the side view of the MoS$_2$ monolayer with the xy mirror-symmetry plane indicated on the Mo layer. Panel (b) depicts the top views of MoS$_2$, including three mirror-symmetry pains and schematics for an interatomic hopping between d$_{xy}$ and d$_{x^2-y^2}$ orbitals of Mo along the x direction. Due to the lack of symmetry, the latter results in a Zeeman-type splitting at the K-point depicted in (c). Panels (d)–(f) showcase ISB of the xy mirror-symmetry plane *via* an external (d) electric field, (e) adsorption, and (f) Janus-type substitution, which can result in Rashba-type splitting near Γ-point as depicted in (g).

plane, the interatomic hopping energy between them becomes non-zero. This leads to the emergence of non-vanishing orbital OAM, characterized by $\langle \hat{L}_x \rangle$ and $\langle \hat{L}_y \rangle$, which in the presence of atomic SOI induces a Rashba-type splitting (see Fig. 10g).

7.4 HgTe and GaAs

Having covered both Rashba and Zeeman-type GSS, it would be prudent to conclude our examples by illustrating how the interorbital-hopping mechanism for non-zero OAM can be applied to Dresselhaus-type splitting in bulk systems.§ Much like the Rashba effect, this phenomenon results in the splitting of energy bands due to spin–orbit interaction in the presence of inversion asymmetry. However, unlike the Rashba effect, where asymmetry typically arises from the spatial inhomogeneity of an interface or surface, the Dresselhaus effect originates from the bulk's inversion asymmetry.[92] With this distinction in mind, it is worth exploring whether such lack of symmetry can also induce non-zero OAM, whether these bands exhibit spin splitting, and if the extent of this effect is linked to the atomic SOI of the elements comprising the crystal structure.

To illustrate this, we will examine the spin splitting of the lowest conduction band in bulk materials characterized by a zinc blende crystal structure. This choice is driven by the fact that zinc blende crystals lack the inversion symmetry required for Dresselhaus-type GSS, and their lowest conduction bands have orbital compositions suitable for the comparative analysis.

Let's begin our inquiry by examining a material comprised of high-atomic-number elements, such as mercury telluride (HgTe). The unit cell of HgTe is illustrated in Fig. 11a. HgTe is a semi-metal related to the II–VI group of semiconductors known for being the first discovered topological insulator.[93] In the vicinity of the Γ point, the lowest conduction band of this material is primarily composed of 5s and 5p orbitals of Te.[75] At the Γ point, where symmetry dictates zero OAM and spin splitting, the electronic states consist solely of s orbitals.

---

§ As mentioned earlier, the effective Hamiltonian in the BR model includes components in the form of $(\sigma_x k_y - \sigma_y k_x)$. However, in cases where the system exhibits higher symmetry (*e.g.*, in bulk), additional terms emerge, leading to the manifestation of the Dresselhaus effect. It's important to emphasize that the point-group symmetry is determined by the subgroup of the k-point. Consequently, the precise relationship between spin and crystal momentum hinges on the specific symmetry characteristics of the crystal.

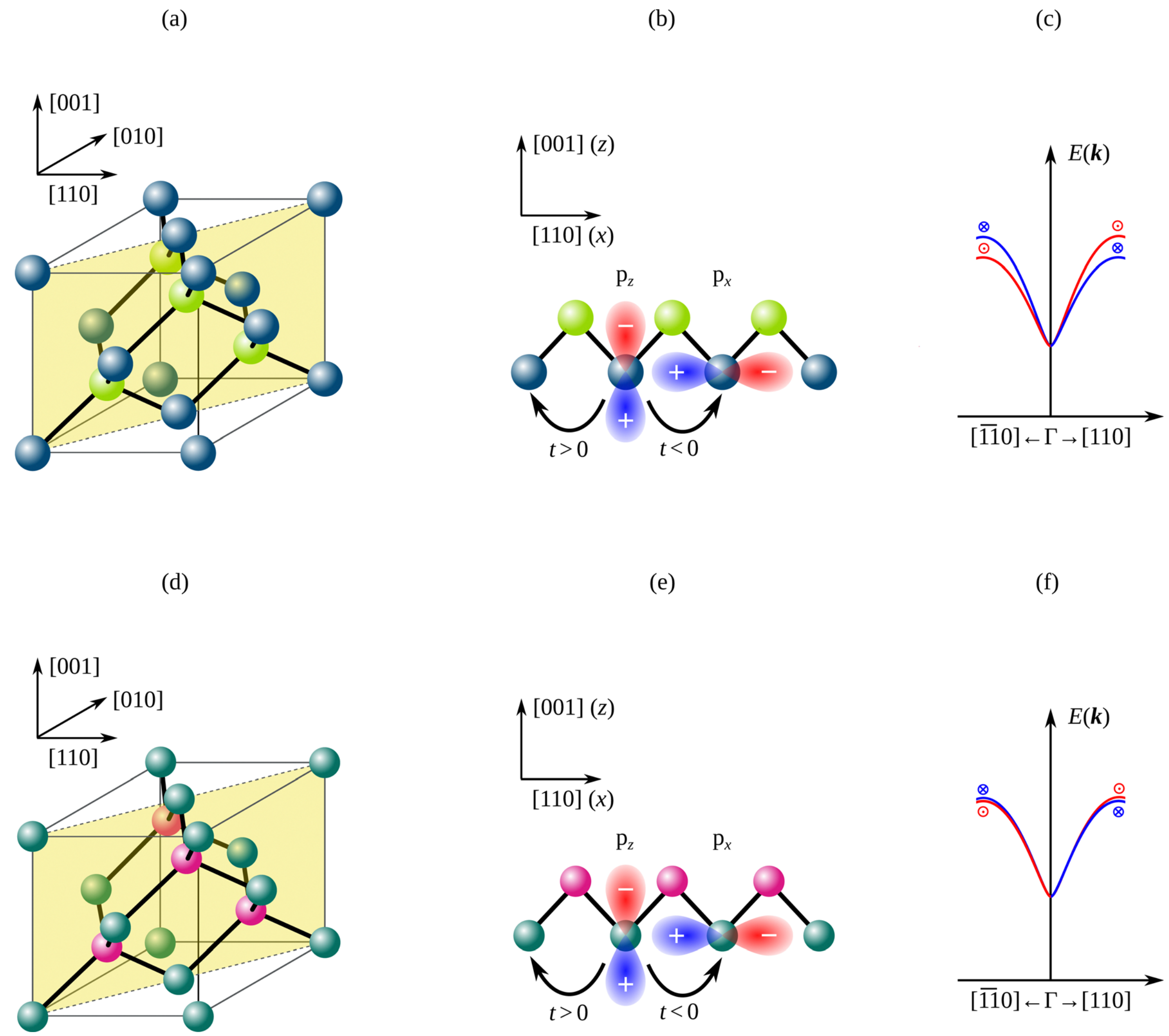

Fig. 11 HgTe structure and electronic bands. Panel (a) illustrates the unit cell of the HgTe with $(\bar{1}10)$ mirror plane is shaded in yellow. The Hg and Te atoms are colored as lime and dark blue, respectively. Panel (b) depicts a schematic representation of the interatomic hopping between p_x and p_y orbitals of Te along [110] direction. Panel (c) shows the spin splitting in the lowest conduction band of HgTe. GaAs structure and electronic bands. The Ga and As atoms are colored as fuchsia and jade, respectively. Panel (e) depicts a schematic representation of the interatomic hopping between p_x and p_y orbitals of As along [110] direction. Panel (f) shows the spin splitting in the lowest conduction band of GaAs.

However, as we move away from this high-symmetry point, crystal field effects come into play. These effects can lead to a momentum-dependent mixing of orthogonal p orbitals of Te, which, in principle, could result in non-zero OAM.

Consequently, let's delve into the symmetries of the zinc blende structure and determine when and how will they affect the OAM. When the momentum vector $\boldsymbol{k}$ is aligned along the [100] direction the OAM and spin splitting in the lowest conduction band will remain zero due to the presence of two mirror planes, (011) and $(01\bar{1})$. Furthermore, the same will hold true for $\boldsymbol{k}$ aligned along the [010] and [001] directions. However, when $\boldsymbol{k}$ is aligned along the [110] direction (for convenience, let's refer to it as the x direction), the $(\bar{1}10)$ plane is the only mirror plane containing the [110] direction. The (001) plane is not a mirror plane due to the presence of Hg atoms positioned above Te atoms, as shown in Fig. 11a. This broken mirror symmetry causes the p_z–p_x hybrid orbitals to be antisymmetric in momentum space, as depicted in Fig. 11b. This leads to non-zero OAM oriented in the $[\bar{1}10]$ (lets refer to it as the y direction), $\langle \hat{L}_y \rangle$, which couples spin *via* strong atomic SOI of Te, contributing to non-zero spin splitting along [110] ($\boldsymbol{k}_x$), as shown in Fig. 11c. Meanwhile, when $\boldsymbol{k}$ is along $[\bar{1}10]$, the arrangement of Hg atoms below Te atoms in the Hg–Te zigzag chain along $[\bar{1}10]$ changes the sign of the hopping energy between p_z and p_y orbitals. This reversal in sign results in a change in the OAM direction, making the OAM dependent on the $\boldsymbol{k}$ direction.

However, what would happen if the atomic SOI was weaker? Would this result in a lower value of spin splitting? Let's explore this by considering a material composed of lower-atomic-number elements compared to HgTe, such as gallium arsenide (GaAs). GaAs is a well-known III–V semiconductor, but it should be noted that other related compounds like InP or InAs could have been considered instead. The lower conduction band of GaAs exhibits a similar dispersion compared to that of HgTe.[75,94] At the Γ point, this band comprises s orbitals of Ga and As. However, due to the crystal structure (refer to Fig. 11d), the same symmetries apply as in the case of HgTe. Hence, along the [110] direction, the crystal field induces momentum-dependent mixing of orthogonal p orbitals, mainly of As origin (as shown in Fig. 11e) Consequently, this leads to a non-zero OAM, which coincides with the spin splitting along the [110] direction. as shown in Fig. 11f. Nevertheless, the atomic SOI in As is weaker compared to Te. As a result, this splitting in GaAs is relatively lower when compared to HgTe.[75,94] Furthermore, a similar argument applies when comparing the splitting along the [110] direction in GaAs and GaSb. In GaSb, the stronger SOI of Sb contributes to a greater magnitude of spin splitting.[94]

8 Giant spin splitting without spin–orbit interaction

In our final comments, it is important to emphasize that not all GSS phenomena are solely a result of strong atomic SOI. In fact, SOI is not a necessary condition for achieving an antisymmetric spin texture in momentum space. The crucial factor is the disruption of rotational symmetry, which ensures that SAM is no longer a conserved quantum number. Apart from SOI, magnetism can also disrupt spin rotational invariance.[95,96] This exchange-induced momentum-dependent spin splitting has been observed in various intrinsic collinear antiferromagnetic materials.[97,98] It is also well established that GSS can be obtained *via* exchange interaction with magnetic impurities or magnetic layers in semiconductor materials.[74,99–101] In these compounds, electron spins align with the magnetic order, making them distinct from the SOI-induced splitting discussed in this review (see discussion elsewhere[19]). Since the chemical composition of these materials also plays a significant role in the formation of GSS, there could be a substantial area of research that pertains to chemical physicists in this field. To achieve a momentum-dependent spin texture, characterized by variations in spin direction across the Brillouin zone, one should consider (antiferro)magnetic materials with non-collinear magnetic structures.[102] The resulting spin texture exhibits symmetries consistent with the underlying magnetic configuration and remains inversion-symmetric. When spatial inversion symmetry is broken in antiferromagnets, it gives rise to antisymmetric spin-momentum locking, as discussed elsewhere.[103]

9 Conclusions

To facilitate the ongoing efforts in the field of spintronics, it is crucial to devise more robust strategies for enhancing spin splitting. Clear guiding principles need to be established to design materials with desired GSS. As a result, it becomes essential to thoroughly characterize and understand spin splitting in new materials. Furthermore, structural modification of these novel platforms must be considered to unlock their full potential for spintronics applications. This endeavor, in turn, captures the interest of numerous young chemists, who, due to the lack of necessary tools, often struggle to accurately account for the atomic SOI in the formation of GSS. This is often facilitated by the interpretation of the spin splitting derived from the original Bychkov–Rashba picture. The model predicts, among other things, spin-degeneracy lifting with a chiral spin structure. However, it fails the predicted energy scale of the band splitting, since it does not consider contributions from atomic SOI.

The role of atomic SOI in the formation of GSS has been well established, paving the way for a more informed exploration of materials with desired spin properties. This exploration often involves taking into consideration the effects of OAM and accounting for its generation. However, since non-vanishing OAM is frequently elucidated within tight-bonding models, its emergence may seem sometimes perplexing or even daunting to grasp for many young researchers interested in spintronics and material research.

Nevertheless, this complexity can be demystified. The most straightforward method to generate an atomic orbital moment involves mixing orthogonal orbitals in the presence of ISB, ensuring that the hybrid is antisymmetric in momentum space. Consequently, by understanding the nature of chemical bonding in the materials, coupled with consideration for the symmetry of the system, and orbital parity, ample insight can be gained into the mechanisms underlying the formation of non-vanishing OAM.

Furthermore, this perspective distinctly highlights that surface interactions hold a substantial significance in facilitating spin splitting. Depending on the specific orbitals involved, these interactions can either suppress or enhance GSS. This insight proves particularly useful for new materials and chemical modification, as it establishes an intuitive connection between GSS and chemical bonding in the presence of ISB, sufficient to understand the mechanism behind non-zero OAM, without the explicit reliance on the tight-binding Hamiltonian. Consequently, this approach can render it more approachable to understand, explore, and exploit the effects of atomic SOI when designing novel materials for spintronics.

Author contributions

Maciej J. Szary: conceptualization, formal analysis, investigation, writing – original draft, writing – review & editing, visualization, supervision, project administration.

Conflicts of interest

There are no conflicts to declare.

Acknowledgements

This work was supported by the Ministry of Education and Science in Poland (Grant No. 0512/ SBAD/2320) within the project realized at the Institute of Physics, Poznan University of Technology.

Notes and references

1 M. Atzori and R. Sessoli, *J. Am. Chem. Soc.*, 2019, **141**, 11339–11352.
2 D. Akinwande, C. Huyghebaert, C.-H. Wang, M. I. Serna, S. Goossens, L.-J. Li, H.-S. P. Wong and F. H. L. Koppens, *Nature*, 2019, **573**, 507–518.
3 S.-J. Liang, B. Cheng, X. Cui and F. Miao, *Adv. Mater.*, 2020, **32**, 1903800.
4 V. Saraswat, R. M. Jacobberger and M. S. Arnold, *ACS Nano*, 2021, **15**, 3674–3708.
5 S. A. Wolf, D. D. Awschalom, R. A. Buhrman, J. M. Daughton, S. von Molnár, M. L. Roukes, A. Y. Chtchelkanova and D. M. Treger, *Science*, 2001, **294**, 1488–1495.
6 S. A. Wolf, A. Y. Chtchelkanova and D. M. Treger, *IBM J. Res. Dev.*, 2006, **50**, 101–110.
7 S. Bhatti, R. Sbiaa, A. Hirohata, H. Ohno, S. Fukami and S. Piramanayagam, *Mater. Today*, 2017, **20**, 530–548.
8 A. Hirohata, K. Yamada, Y. Nakatani, I.-L. Prejbeanu, B. Diény, P. Pirro and B. Hillebrands, *J. Magn. Magn. Mater.*, 2020, **509**, 166711.
9 X. Wang, Z. Cheng, G. Zhang, H. Yuan, H. Chen and X.-L. Wang, *Phys. Rep.*, 2020, **888**, 1–57.
10 Y. Huang, V. Polojärvi, S. Hiura, P. Höjer, A. Aho, R. Isoaho, T. Hakkarainen, M. Guina, S. Sato, J. Takayama, A. Murayama, I. A. Buyanova and W. M. Chen, *Nat. Photonics*, 2021, **15**, 475–482.
11 M. Ramsteiner, O. Brandt, T. Flissikowski, H. T. Grahn, M. Hashimoto, J. Herfort and H. Kostial, *Phys. Rev. B: Condens. Matter Mater. Phys.*, 2008, **78**, 121303.
12 M. Gurram, S. Omar and B. J. V. Wees, *Nat. Commun.*, 2017, **8**, 248.
13 K. Yaji, Y. Ohtsubo, S. Hatta, H. Okuyama, K. Miyamoto, T. Okuda, A. Kimura, H. Namatame, M. Taniguchi and T. Aruga, *Nat. Commun.*, 2010, **1**, 17.
14 H. C. Koo, S. B. Kim, H. Kim, T.-E. Park, J. W. Choi, K.-W. Kim, G. Go, J. H. Oh, D.-K. Lee, E.-S. Park, I.-S. Hong and K.-J. Lee, *Adv. Mater.*, 2020, **32**, 2002117.
15 K. Yasuda, H. Yasuda, T. Liang, R. Yoshimi, A. Tsukazaki, K. S. Takahashi, N. Nagaosa, M. Kawasaki and Y. Tokura, *Nat. Commun.*, 2019, **10**, 2734.
16 Y. M. Itahashi, T. Ideue, Y. Saito, S. Shimizu, T. Ouchi, T. Nojima and Y. Iwasa, *Sci. Adv.*, 2020, **6**, eaay9120.
17 J. B. S. Mendes, M. Gamino, R. O. Cunha, J. E. Abrão, S. M. Rezende and A. Azevedo, *Phys. Rev. Mater.*, 2021, **5**, 024206.
18 S. Varotto, L. Nessi, S. Cecchi, J. Sławińska, P. Noël, S. Petrò, F. Fagiani, A. Novati, M. Cantoni, D. Petti, E. Albisetti, M. Costa, R. Calarco, M. Buongiorno Nardelli, M. Bibes, S. Picozzi, J.-P. Attané, L. Vila, R. Bertacco and C. Rinaldi, *Nat. Electron.*, 2021, **4**, 740–747.
19 G. Bihlmayer, P. Noël, D. V. Vyalikh, E. V. Chulkov and A. Manchon, *Nat. Rev. Phys.*, 2022, **4**, 642–659.
20 A. Manchon, H. C. Koo, J. Nitta, S. M. Frolov and R. A. Duine, *Nat. Mater.*, 2015, **14**, 871–882.
21 D. Bercioux and P. Lucignano, *Rep. Prog. Phys.*, 2015, **78**, 106001.
22 M. S. Bahramy and N. Ogawa, *Adv. Mater.*, 2017, **29**, 1605911.
23 T. Uchihashi, *AAPPS Bull.*, 2021, **31**, 27.
24 Y. A. Bychkov and E. I. Rashba, *JETP Lett.*, 1984, **39**, 78–81.
25 S. LaShell, B. McDougall and E. Jensen, *Phys. Rev. Lett.*, 1996, **77**, 3419–3422.
26 M. Hoesch, M. Muntwiler, V. N. Petrov, M. Hengsberger, L. Patthey, M. Shi, M. Falub, T. Greber and J. Osterwalder, *Phys. Rev. B: Condens. Matter Mater. Phys.*, 2004, **69**, 241401.
27 D. Pacilé, C. R. Ast, M. Papagno, C. Da Silva, L. Moreschini, M. Falub, A. P. Seitsonen and M. Grioni, *Phys. Rev. B: Condens. Matter Mater. Phys.*, 2006, **73**, 245429.
28 C. R. Ast, J. Henk, A. Ernst, L. Moreschini, M. C. Falub, D. Pacilé, P. Bruno, K. Kern and M. Grioni, *Phys. Rev. Lett.*, 2007, **98**, 186807.
29 T. Oguchi and T. Shishidou, *J. Phys.: Condens. Matter*, 2009, **21**, 092001.
30 A. Nuber, J. Braun, F. Forster, J. Minár, F. Reinert and H. Ebert, *Phys. Rev. B: Condens. Matter Mater. Phys.*, 2011, **83**, 165401.
31 S. N. P. Wissing, C. Eibl, A. Zumbülte, A. B. Schmidt, J. Braun, J. Minár, H. Ebert and M. Donath, *New J. Phys.*, 2013, **15**, 105001.
32 G. A. Khodaparast, R. E. Doezema, S. J. Chung, K. J. Goldammer and M. B. Santos, *Phys. Rev. B: Condens. Matter Mater. Phys.*, 2004, **70**, 155322.
33 T. Nakagawa, O. Ohgami, Y. Saito, H. Okuyama, M. Nishijima and T. Aruga, *Phys. Rev. B: Condens. Matter Mater. Phys.*, 2007, **75**, 155409.
34 K. Yaji, A. Harasawa, K. Kuroda, R. Li, B. Yan, F. Komori and S. Shin, *Phys. Rev. B*, 2018, **98**, 041404.
35 M. Nagano, A. Kodama, T. Shishidou and T. Oguchi, *J. Phys.: Condens. Matter*, 2009, **21**, 064239.
36 I. Gierz, T. Suzuki, E. Frantzeskakis, S. Pons, S. Ostanin, A. Ernst, J. Henk, M. Grioni, K. Kern and C. R. Ast, *Phys. Rev. Lett.*, 2009, **103**, 046803.
37 K. Sakamoto, T. Oda, A. Kimura, K. Miyamoto, M. Tsujikawa, A. Imai, N. Ueno, H. Namatame, M. Taniguchi, P. E. J. Eriksson and R. I. G. Uhrberg, *Phys. Rev. Lett.*, 2009, **102**, 096805.
38 B. Pieczyrak, M. Szary, L. Jurczyszyn and M. W. Radny, *Phys. Rev. B*, 2016, **93**, 195318.
39 Y. M. Koroteev, G. Bihlmayer, J. E. Gayone, E. V. Chulkov, S. Blügel, P. M. Echenique and P. Hofmann, *Phys. Rev. Lett.*, 2004, **93**, 046403.
40 O. Krupin, G. Bihlmayer, K. Starke, S. Gorovikov, J. E. Prieto, K. Döbrich, S. Blügel and G. Kaindl, *Phys. Rev. B: Condens. Matter Mater. Phys.*, 2005, **71**, 201403.
41 M. Hochstrasser, J. G. Tobin, E. Rotenberg and S. D. Kevan, *Phys. Rev. Lett.*, 2002, **89**, 216802.
42 M. H. Berntsen, O. Götberg and O. Tjernberg, *Phys. Rev. B*, 2018, **97**, 125148.
43 S. Hatta, T. Aruga, Y. Ohtsubo and H. Okuyama, *Phys. Rev. B: Condens. Matter Mater. Phys.*, 2009, **80**, 113309.
44 S. Hatta, T. Aruga, C. Kato, S. Takahashi, H. Okuyama, A. Harasawa, T. Okuda and T. Kinoshita, *Phys. Rev. B: Condens. Matter Mater. Phys.*, 2008, **77**, 245436.

45 A. V. Matetskiy, S. Ichinokura, L. V. Bondarenko, A. Y. Tupchaya, D. V. Gruznev, A. V. Zotov, A. A. Saranin, R. Hobara, A. Takayama and S. Hasegawa, *Phys. Rev. Lett.*, 2015, **115**, 147003.

46 K. Taguchi, K. Sumida, Y. Okuda, K. Miyamoto, A. Kimura, T. Oguchi and T. Okuda, *Phys. Rev. B*, 2020, **101**, 045430.

47 W. Ju, D. Wang, T. Li, Y. Zhang, Z. Gao, L. Ren, H. Li and S. Gong, *Phys. Chem. Chem. Phys.*, 2020, **22**, 9148–9156.

48 L. Chi, C. V. Singh and J. Nogami, *Nanoscale*, 2021, **13**, 16622–16628.

49 A. Mihalyuk, L. Bondarenko, A. Tupchaya, T. Utas, J.-P. Chou, D. Gruznev, S. Eremeev, A. Zotov and A. Saranin, *Nanoscale*, 2022, **14**, 11227–11234.

50 S. Zhang, F. Wang, B. Cui, C. Li and Y. Jia, *Phys. Lett. A*, 2023, **479**, 128920.

51 S. Oh and H. J. Choi, *Sci. Rep.*, 2017, **7**, 2024.

52 M. J. Szary, M. T. Michalewicz and M. W. Radny, *Appl. Surf. Sci.*, 2019, **494**, 619–626.

53 L. Yuan, Q. Liu, X. Zhang, J.-W. Luo, S.-S. Li and A. Zunger, *Nat. Commun.*, 2019, **10**, 906.

54 S. Gupta and B. I. Yakobson, *J. Am. Chem. Soc.*, 2021, **143**, 3503–3508.

55 F. Sattari and S. Mirershadi, *Sci. Rep.*, 2021, **11**, 17617.

56 Q. Peng, Y. Lei, X. Deng, J. Deng, G. Wu, J. Li, C. He and J. Zhong, *Phys. E*, 2022, **135**, 114944.

57 F. Sattari, *J. Phys. Chem. Solids*, 2023, **182**, 111567.

58 H. Lind, J. Halim, S. I. Simak and J. Rosen, *Phys. Rev. Mater.*, 2017, **1**, 044002.

59 R. Meshkian, H. Lind, J. Halim, A. El Ghazaly, J. Thörnberg, Q. Tao, M. Dahlqvist, J. Palisaitis, P. O. A. Persson and J. Rosen, *ACS Appl. Nano Mater.*, 2019, **2**, 6209–6219.

60 H. U. Din, M. Idrees, A. Albar, M. Shafiq, I. Ahmad, C. V. Nguyen and B. Amin, *Phys. Rev. B*, 2019, **100**, 165425.

61 S.-D. Guo, W.-Q. Mu, Y.-T. Zhu, R.-Y. Han and W.-C. Ren, *J. Mater. Chem. C*, 2021, **9**, 2464–2473.

62 D. Ghosh, K. Roy, S. Maitra and P. Kumar, *J. Phys. Chem. Lett.*, 2022, **13**, 1234–1240.

63 C. Xin, Z. Fan, Z. Sun, H. Li, G. Jin, F. Pan and Y. Sui, *Phys. Chem. Chem. Phys.*, 2023, **25**, 8676–8683.

64 W. Wei, Y. Dai, C. Niu, X. Li, Y. Ma and B. Huang, *J. Mater. Chem. C*, 2015, **3**, 11548–11554.

65 M. J. Szary, *FlatChem*, 2019, **18**, 100141.

66 M. J. Szary, *Surf. Sci.*, 2020, **697**, 121604.

67 S. B. Touski and N. Ghobadi, *J. Phys. D: Appl. Phys.*, 2021, **54**, 485302.

68 D. Fang, S. Chen, Y. Li and B. Monserrat, *J. Phys.: Condens. Matter*, 2021, **33**, 155001.

69 Y. Li, X. Xu, M. Lan, S. Wang, T. Huang, H. Wu, F. Li and Y. Pu, *Phys. Chem. Chem. Phys.*, 2022, **24**, 25962–25968.

70 Y. Li, M. Lan, S. Wang, T. Huang, Y. Chen, H. Wu, F. Li and Y. Pu, *Phys. Chem. Chem. Phys.*, 2023, **25**, 15676–15682.

71 N. Li, Q. Xia, W.-X. Ji, M. Ding, M.-J. Ren, P.-J. Wang, P. Li, S.-F. Zhang and S.-S. Li, *Phys. E*, 2023, **148**, 115654.

72 B. D. Bhat, *J. Phys.: Condens. Matter*, 2023, **35**, 435301.

73 A. M. Hoque, V. Ramachandra, A. George, E. Najafidehaghani, Z. Gan, R. Mitra, B. Zhao, D. Khokhriakov, A. Turchanin, S. Lara-Avila, S. Kubatkin and S. P. Dash, *Phys. Rev. Mater.*, 2023, **7**, 044005.

74 Y. G. Semenov, X. Duan and K. W. Kim, *Phys. Rev. B: Condens. Matter Mater. Phys.*, 2012, **86**, 161406.

75 R. Islam, B. Ghosh, G. Cuono, A. Lau, W. Brzezicki, A. Bansil, A. Agarwal, B. Singh, T. Dietl and C. Autieri, *Phys. Rev. Res.*, 2022, **4**, 023114.

76 M. J. Szary, B. Pieczyrak, L. Jurczyszyn and M. W. Radny, *Appl. Surf. Sci.*, 2019, **466**, 224–229.

77 S. R. Park, C. H. Kim, J. Yu, J. H. Han and C. Kim, *Phys. Rev. Lett.*, 2011, **107**, 156803.

78 B. Kim, P. Kim, W. Jung, Y. Kim, Y. Koh, W. Kyung, J. Park, M. Matsunami, S.-I. Kimura, J. S. Kim, J. H. Han and C. Kim, *Phys. Rev. B: Condens. Matter Mater. Phys.*, 2013, **88**, 205408.

79 J.-H. Park, C. H. Kim, J.-W. Rhim and J. H. Han, *Phys. Rev. B: Condens. Matter Mater. Phys.*, 2012, **85**, 195401.

80 B. Kim, C. H. Kim, P. Kim, W. Jung, Y. Kim, Y. Koh, M. Arita, K. Shimada, H. Namatame, M. Taniguchi, J. Yu and C. Kim, *Phys. Rev. B: Condens. Matter Mater. Phys.*, 2012, **85**, 195402.

81 L. Petersen and P. HedegÅrd, *Surf. Sci.*, 2000, **459**, 49–56.

82 M. Kim, J. Im, A. J. Freeman, J. Ihm and H. Jin, *Proc. Natl. Acad. Sci. U. S. A.*, 2014, **111**, 6900–6904.

83 C. K. Safeer, J. Ingla-Aynés, F. Herling, J. H. Garcia, M. Vila, N. Ontoso, M. R. Calvo, S. Roche, L. E. Hueso and F. Casanova, *Nano Lett.*, 2019, **19**, 1074–1082.

84 J. Ingla-Aynés, F. Herling, J. Fabian, L. E. Hueso and F. Casanova, *Phys. Rev. Lett.*, 2021, **127**, 047202.

85 F. Calavalle, M. Suárez-Rodríguez, B. Martín-García, A. Johansson, D. C. Vaz, H. Yang, I. V. Maznichenko, S. Ostanin, A. Mateo-Alonso, A. Chuvilin, I. Mertig, M. Gobbi, F. Casanova and L. E. Hueso, *Nat. Mater.*, 2022, **21**, 526–532.

86 J. Ingla-Aynés, I. Groen, F. Herling, N. Ontoso, C. K. Safeer, F. de Juan, L. E. Hueso, M. Gobbi and F. Casanova, *2D Mater.*, 2022, **9**, 045001.

87 N. Alidoust, G. Bian, S.-Y. Xu, R. Sankar, M. Neupane, C. Liu, I. Belopolski, D.-X. Qu, J. D. Denlinger, F.-C. Chou and M. Z. Hasan, *Nat. Commun.*, 2014, **5**, 4673.

88 Y. Zhang, H. Li, H. Wang, R. Liu, S.-L. Zhang and Z.-J. Qiu, *ACS Nano*, 2015, **9**, 8514–8519.

89 S. C. de la Barrera, M. R. Sinko, D. P. Gopalan, N. Sivadas, K. L. Seyler, K. Watanabe, T. Taniguchi, A. W. Tsen, X. Xu, D. Xiao and B. M. Hunt, *Nat. Commun.*, 2018, **9**, 1427.

90 M. J. Szary, *Appl. Surf. Sci.*, 2019, **491**, 469–477.

91 H. Nakamura, A. Mohammed, P. Rosenzweig, K. Matsuda, K. Nowakowski, K. Küster, P. Wochner, S. Ibrahimkutty, U. Wedig, H. Hussain, J. Rawle, C. Nicklin, B. Stuhlhofer, G. Cristiani, G. Logvenov, H. Takagi and U. Starke, *Phys. Rev. B*, 2020, **101**, 165103.

92 G. Dresselhaus, *Phys. Rev.*, 1955, **100**, 580–586.

93 M. König, S. Wiedmann, C. Brüne, A. Roth, H. Buhmann, L. W. Molenkamp, X.-L. Qi and S.-C. Zhang, *Science*, 2007, **318**, 766–770.

94 M. Gmitra and J. Fabian, *Phys. Rev. B*, 2016, **94**, 165202.

95 L.-D. Yuan, Z. Wang, J.-W. Luo, E. I. Rashba and A. Zunger, *Phys. Rev. B*, 2020, **102**, 014422.

96 L.-D. Yuan, Z. Wang, J.-W. Luo and A. Zunger, *Phys. Rev. Mater.*, 2021, **5**, 014409.
97 L. Šmejkal, R. González-Hernández, T. Jungwirth and J. Sinova, *Sci. Adv.*, 2020, **6**, eaaz8809.
98 R. González-Hernández, L. S. Šmejkal, K. Výborný, Y. Yahagi, J. Sinova, T. C. V. Jungwirth and J. Z. Železný, *Phys. Rev. Lett.*, 2021, **126**, 127701.
99 T. Dietl, H. Ohno and F. Matsukura, *Phys. Rev. B: Condens. Matter Mater. Phys.*, 2001, **63**, 195205.
100 J. A. Gaj and J. Kossut, in *Basic Consequences of sp-d and d-d Interactions in DMS*, ed. J. A. Gaj and J. Kossut, Springer Berlin Heidelberg, Berlin, Heidelberg, 2010, pp. 1–36.
101 T. Dietl and H. Ohno, *Rev. Mod. Phys.*, 2014, **86**, 187–251.
102 J. Z. Železný, Y. Zhang, C. Felser and B. Yan, *Phys. Rev. Lett.*, 2017, **119**, 187204.
103 S. Hayami, Y. Yanagi and H. Kusunose, *Phys. Rev. B*, 2020, **101**, 220403.